Windage loss characterisation for flywheel energy storage system: Model and experimental validation

Energy 307 (2024) 132641

Contents lists available at ScienceDirect

Energy

journal homepage: www.elsevier.com/locate/energy

Windage loss characterisation for flywheel energy storage system: Model and experimental validation

Simone Venturini *, Salvatore Paolo Cavallaro, Alessandro Vigliani

Department of Mechanical and Aerospace Engineering, Politecnico di Torino, Corso Duca degli Abruzzi, 24, Torino, 10129, Italy

ARTICLE INFO

Keywords:
Vertical rotor
Aerodynamic loss
Vacuum

ABSTRACT

In this paper, a windage loss characterisation strategy for Flywheel Energy Storage Systems (FESS) is presented. An effective windage loss modelling in FESS is essential for feasible and competitive design. Unlike generic aerodynamic loss models, FESS require particular attention to their unique characteristics i.e., vacuum, small airgaps, high angular speed, and presence of low friction rotor supports.

The proposed model is based on several analytical and semi-empirical windage loss solutions for cylindrical and planar surface interactions, harmonised to manage the transition between laminar and turbulent flows. Also, the model is enriched by introducing corrections for rarefied gasses, using kinetic gas theory formulation. Therefore, it is possible the reduce the windage overestimation occurring with Navier–Stokes equation solutions for laminar flow. The model is compared to case studies from the literature featuring different boundary and operating conditions, to check consistency of all the harmonised models. A dedicated experimental test-rig is developed to validate the corrections to the model for rarefied gas at different vacuum levels. Then, a non-invasive characterisation approach for FESS windage losses in self-discharge phase is proposed and validated on the test-rig.

1. Introduction

Flywheel Energy Storage Systems (FESS) have attracted significant attention in the sustainable energy storage ecosystem, where is crucial developing environmentally friendly methods for sourcing materials, manufacturing processes, and end-of-life management [1].

FESS are notable for their high round-trip efficiency, power density, and rapid response time, making them suitable for applications such as grid stabilisation and frequency regulation [2], renewable energy integration [3], microgrid support and islanding [4,5], Uninterruptible Power Supply (UPS) [6,7], electric vehicle charging infrastructure [8], aerospace applications [9,10], and nuclear energy applications [11,12].

Currently, the primary challenges in FESS technology are reducing energy costs, increasing energy density, and improving daily discharge capacity. In a recent review about energy storage systems, Mitali et al. [13] highlighted that high speed FESS current Technology Readiness Level (TRL) is about 5–7 and that the energy density range is $5 \div 80$ Wh/kg, and the discharge time is in the order of minutes.

The challenge of reducing energy costs in FESS has been addressed by replacing full composite material flywheel solutions [14–16] with more cost effective mixed material solutions, such as steel shafts combined with localised Carbon Fibre Reinforced Polymer (CFRP) composites [17,18].

Enhancing energy density has primarily involved optimising the flywheel shape profile to maximise the peripheral mass distribution. Several manufacturers have introduced disc-rim profiles. For example, in 2013, GKN developed GyroDrive Mk4, a non-symmetric disc-rim profile FESS [19]. In the next years, Beacon Power and Powerthru developed symmetric disc-rim profile FESS using a steel-CFRP material composition [17,18].

Recently, these solutions have been abandoned in favour of shaftless configurations [16,20,21]. Transitioning from disc-rim to shaftless flywheel architecture increases the wet surface interacting with the housing fluid, leading to higher windage losses. The common solution to reduce the windage losses involves reducing the chamber pressure to achieve a free molecule flow, typically using high-vacuum level solutions [14–21]. Despite high-vacuum environment solution effectiveness, the energy cost balance must be carefully analysed.

Another approach is to design FESS to optimise rotor windage loss. The study of windage losses is crucial not only for improving daily discharge capacity, but also for addressing other technological requirements. For instance, CFRP materials experience a reduction in mechanical properties at high temperatures due to aerodynamic heating [22]. In 1997, Kolk developed a FESS for grid applications with a 10^{-2} Pa vacuum using a 2-stage turbomolecular pump [23].

* Corresponding author.
E-mail address: simone.venturini@polito.it (S. Venturini).

https://doi.org/10.1016/j.energy.2024.132641
Received 19 March 2024; Received in revised form 18 July 2024; Accepted 27 July 2024
Available online 30 July 2024

Kolk does not supply further details on windage losses, but justifies the low pressure with CFRP material limitations around 140 °C. Similarly, Quurk et al. imposed 10^{-2} Pa vacuum pressure through turbomolecular pump [20].

FESS windage losses cannot be modelled as generic aerodynamic losses in turbulent flow [24], due to several specific characteristics:

- *small airgaps*: the aerodynamic loss boundary layer and the flow regime are affected by the dimensions of the interacting surfaces;
- *centrifugal forces*: the rotation of the interacting surfaces requires considering also the contribution of centrifugal forces acting on the fluid bringing vortex instability depending on the operating conditions [25];
- *cylindrical and annular interactions:* the frontal channel boundary layer considerations must be reconsidered for different geometry of interacting surfaces, thus requiring, at least in laminar flow, a different approach to the integration of Navier–Stokes Equations (NSE);
- *gas rarefaction*: for high vacuum level, NSE solution hypotheses of continuum flow are not consistent. Therefore, the NSE solution is corrected using gas kinetic theory considerations to consider slip and free molecule flows [26].

The correction for gas rarefaction using gas kinetic theory is proposed in [27] using the Gu solution [28], which is limited to annular interaction only. The NSE solution for continuum flow is commonly found in boundary layer theory textbooks [25,29,30] for interacting cylindrical surfaces.

In 2003, Liu et al. [31] implemented kinetic gas theory to predict windage losses of enclosed rotors in the pressure range of $1.\overline{3} \times \left(10^{1} \div 10^{3}\right)$ Pa, obtaining slightly overestimated results in steady-state conditions. The analysis also indicated critical temperature rise at high pressure [32]. This methodology has been adopted by other researchers in FESS application [33]. In 2005, Suzuki et al. [7] tested gaseous mixtures to reduce aerodynamic losses, by considering different helium concentration levels in the power balance, which showed an effective reduction of windage losses.

In 2021, Barkova and Pugachuk [34] performed a comparison between Computational Fluid Dynamics (CFD) and semi-empirical models to investigate the effect of the chamber pressure in FESS applications. The comparison shows that the semi-empirical model is underestimating the power losses and the difference increases at higher rotor velocities.

In 2019, Wei et al. [35] explored various separation techniques to indirectly measure windage losses, proposing several semi-empirical models that proved consistent for vacuum pressures below 2×10^{3} Pa. In 2020, Amiryar and Pullen [36] examined multiple loss contributions and developed a semi-empirical solution applicable down to 10^{-2} Pa, based on Couette flow considerations regarding wall shear stress distribution.

In 2021, Skinner et al. [37] characterised the losses of a FESS 1 kWh barrel-type flywheel demonstrator in the pressure range $27 \div 1333$ Pa. The demonstrator aerodynamic losses were modelled with different semi-empirical models for disc and cylindrical surfaces showing difficulties in separating loss contributions due to the bearings and the electrical machine. In the end, the semi-empirical models are only adopted to identify the dependence of aerodynamic loss terms on angular velocity and then fitted in post-processing.

In FESS application, increasing flywheel external diameter and angular speed improves the flywheel energy density and amplifies centrifugal forces acting on the fluid in the outer airgap. The centrifugal forces lead to Taylor vortex instability, a significant phenomenon in recent FESS technology. Eltaweel et al. [38] evaluated the standby power of a FESS using CFD simulations and analysis of variance, showing that the external airgap must be minimised to reduce aerodynamic losses. In the case studies, the Taylor vortex size reduces size with the airgap. Similarly, Motaman et al. [39] performed CFD analysis on a barrel-type flywheel and identified the critical Taylor number between stable and turbulent Taylor vortexes.

Semi-empirical models are particularly useful for analysing turbulent flow behaviour. Pozzi et al. [40] and Sirigu et al. [41] investigated the fluidic interactions of rotor configurations, both in free and in-housing environments.

From the literature review analysis, it emerges the lack of a unified windage loss model practically useable for rotors with complex geometry and differentiated airgaps. Therefore, this paper presents a complete windage loss model with the following characteristics:

- collection and harmonisation of analytical [25] and semi-empirical solutions [42–45] for boundary conditions typical of FESS applications e.g., small airgaps, fixed stator surfaces, constant operating temperature and vacuum pressure, no air flow rate. The usage of analytical solutions is prioritised for laminar flow, while semi-empirical solutions are adopted to reduce computational costs;
- gas rarefaction corrections to manage the low pressure of the gas in the housing up to 10^{-2} Pa for high Knudsen number values;
- a wide range of boundary and operating conditions to encompass various operational scenarios.

This paper presents the following points of novelty:

- the development of a completely harmonised windage loss model, covering different laminar and turbulent flows, pressure levels, and wide range of airgaps;
- the development of a dedicated experimental test-rig to validate the proposed model for wide ranges of airgaps, speed, and pressure;
- the implementation of an experimental, non-invasive procedure to characterise windage loss under transient conditions.

The proposed methodology is based on the following assumptions:

- the temperature of the system analysed is considered stationary;
- the rotor and stator geometry are considered axisymmetric;
- the rotor and stator geometry are represented only by cylindrical and annular surfaces.

The paper is organised in six sections.

In Section 2, the fundamental windage loss concepts behind NSE and semi-empirical solutions are proposed. In Section 3, the gas rarefaction corrections based on kinetic theory of gasses are introduced in a harmonised windage loss model. In Section 3.3, a windage loss characterisation applicable during FESS self-discharge phase is defined. In Section 4, the model is validated in steady-state conditions using several case studies from the literature, and the results are discussed. In Section 5, the transient windage loss characterisation is performed on a dedicated experimental test-rig comparing the model prediction. The results are discussed. Finally, in Section 6, the outcomes of this research activity are drawn and possible future developments are proposed.

2. Theoretical background

The windage power loss of rotating devices is strictly related to the rotor geometry, the presence of airgaps between the rotor and the housing, temperature, viscosity and density of the interacting fluid, and the rotor speed.

By assuming that the rotor and the housing are axisymmetric, coaxial, without continuous variation of radii, and the rotor is torsionally rigid, the total windage power loss P_w is calculated as the summation of all the rotor drag contributions i.e., $P_{w,C}$ and $P_{w,A}$ drags by cylindrical and annular wet surfaces:

$$P_w = \sum P_{w,C} + \sum P_{w,A} = \left(\sum T_{w,C} + \sum T_{w,A}\right) \Omega \tag{1}$$

in which $T_{w,C}$ and $T_{w,A}$ are the induced torques on the rotor caused by the fluidic interactions of cylindrical and annular wet surfaces, and Ω is

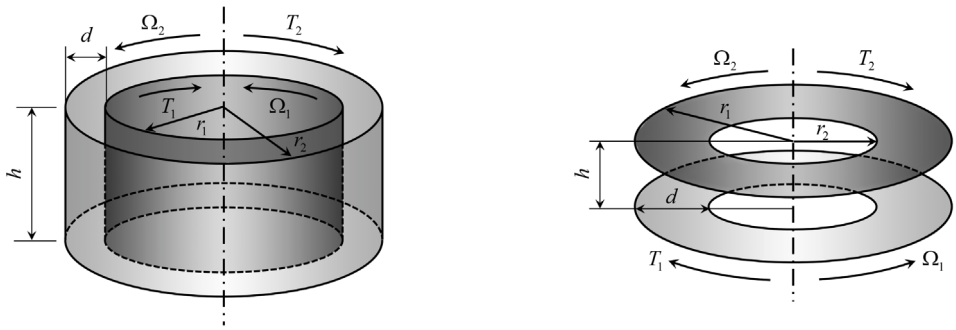

(a) Cylindrical surface interaction. (b) Annular surface interaction.

Fig. 1. Surface interaction schemes.

the rotor angular speed. Fig. 1 shows the geometrical and operational characteristics of cylinders and rings, with the adopted torque and speed conventions.

In both figures, the interacting surfaces have speeds Ω_1 and Ω_2, and corresponding windage torques due to fluid interaction, T_1 and T_2. On the left, the cylinder surfaces have the same height h, and different radii r_1 and r_2, on the right, h indicates the surface airgap, while r_1 and r_2 are the inner and outer radii.

The characteristic length is $d = r_2 - r_1$ and the non-dimensional aspect ratio is $G = d/r$ where r is the largest radius of the rotor surface.

In FESS applications, the stator speed is null. In the case of laminar interaction of the rotor cylindrical surface 1 with the housing surface 2, $\Omega_2 = 0$ and the windage torque T_1 is obtained by the exact solution of NSE for continuum flow [25,29,30]:

$$T_1 = \tau \left(2\pi r_1 h\right) r_1 \tag{2}$$

where τ is the tangential wall shear stress.

If the flow is turbulent, the semi-empirical approach, based on non-dimensional numbers [46], is adopted:

$$T_1 = \frac{1}{2}\pi\rho C_M \Omega_1^2 r_1^4 h \tag{3}$$

which depends on the fluid density ρ, and the moment coefficient C_M. If the rotor is enclosed, the moment coefficient C_M is

$$C_M = f\left(\mathrm{Ta}, \mathrm{Re}_{\phi m}\right) \tag{4}$$

where Ta is the non-dimensional Taylor number (Eq. (5)), identifying the radial flow due to centrifugal to viscous force ratio, and $\mathrm{Re}_{\phi m}$ is the non-dimensional Reynolds number (Eq. (6)), identifying the tangential flow due to inertial to viscous forces ratio [25]

$$\mathrm{Ta} = \frac{\rho}{\mu}\Omega_1 r_1 d\sqrt{\frac{d}{r_1}} = \frac{\rho}{\mu}\Omega_1 r_1 d\sqrt{G_1} \tag{5}$$

$$\mathrm{Re}_{\phi m} = \frac{\rho}{\mu}\Omega_1 r_1 d = \frac{\mathrm{Ta}}{\sqrt{G_1}} \tag{6}$$

where μ is the fluid dynamic viscosity under operational conditions. In this paper, Sutherland's law is adopted to define dynamic viscosity for dry air [26].

If the rotor is in free environment, the moment coefficient C_M is

$$C_M = f\left(\mathrm{Re}_{\phi}\right) \tag{7}$$

where Re_{ϕ} is the non-dimensional Reynolds number (Eq. (8)), identifying the tangential flow due to inertial to viscous forces ratio [25]:

$$\mathrm{Re}_{\phi} = \frac{\rho}{\mu}\Omega_1 r_1^2. \tag{8}$$

In case of laminar interaction of the rotor annular surface 1 with the housing surface 2, $\Omega_2 = 0$ and the induced torque T_1 is obtained by the exact solution of NSE in case of continuum flow [30]:

$$T_1 = 2\pi \int_{r_1}^{r_2} r^2 \tau dr \tag{9}$$

where τ is the wall shear stress.

Similarly to the case presented in Eq. (2), if the flow is turbulent, the semi-empirical approach is adopted:

$$T_1 = \frac{1}{2}\rho\Omega^2 \left[C_M(r_2) r_2^5 - C_M(r_1) r_1^5\right] \tag{10}$$

which depends on the moment coefficient C_M computed at inner and outer radii r_1 and r_2. The moment coefficient C_M is a function of Re_{ϕ} both in enclosed and free environment. Re_{ϕ} is calculated with Eq. (8) for r_1 and r_2. A detailed list of the adopted models in this paper is available in Appendix.

3. Gas rarefaction correction

In FESS application, the housing pressure is drastically reduced to minimise windage power losses. The analytical and semi-empirical models proposed in Section 2 are limited to continuum flow condition.

The analytical models based on NSE represent laminar flow exact solutions when the non-dimensional Knudsen number Kn is much lower than 1. Kn is used to classify the laminar flow depending on the ratio between the mean free path distance λ and the characteristic length d of the phenomenon [26]. The gas rarefaction can be embedded in the NSE solutions by introducing additional fluid behaviour through Kn.

A compressible ideal gas behaviour can be described by the ideal gas law linking pressure p, density ρ, and temperature T [26]. The fluid dynamic viscosity is expressed as a function of the fluid density:

$$\mu \simeq \frac{1}{2}\rho\bar{v}\lambda \tag{11}$$

where $\bar{v}$ is the mean particle speed. By considering a Maxwellian particle velocity distribution $\bar{v}$, λ can be expressed as:

$$\lambda = \frac{\mu}{\rho}\sqrt{\frac{\pi}{2\bar{R}T}} \tag{12}$$

where $\bar{R}$ is the specific gas constant.

In the next subsections, the gas rarefaction correction is introduced into the NSE solution for cylinder and ring surface interaction, also comparing existing formulations in the literature.

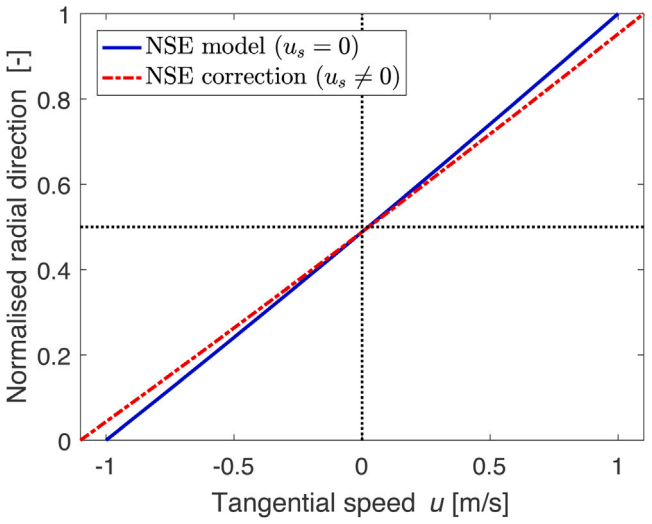

Fig. 2. Cylindrical laminar flow velocity profile solution for $u_2 = -u_1$.

3.1. Cylindrical laminar flow

The Taylor NSE solution [25] is considered, assuming thatthe stator cylindrical surface is not rotating i.e., $r = r_1$, $\Omega_2 = 0$, and the flow is continuous; it holds:

$$|\tau| = 2\mu \frac{r_2^2}{r_2^2 - r_1^2} \Omega_1. \tag{13}$$

The dynamic viscosity in Eq. (13) can be described with the kinetic gas theory for diluted gases; substituting Eq. (12) in Eq. (13) it yields:

$$|\tau| = 2\rho \sqrt{\frac{2\bar{R}T}{\pi}} \Omega_1 r_1 \mathrm{Kn} C_0 \tag{14}$$

with $C_0 = \frac{(1+G)^2}{2+G}$. Eq. (14) is not consistent in continuum flow, i.e., when $\mathrm{Kn} \to 0$. Additionally, inconsistencies are observed in Liu et al. @solution [31]. The solution converges to the expected continuum flow solution, but shows two significant differences from Eq. (14):

- the constant factor 2 is absent, therefore Liu et al. solution is smaller in amplitude with respect to the analytical solution;
- the geometrical dependency from airgap and radius is not quadratic.

The analytical cylindrical laminar flow solution is corrected assuming non-null tangential slip velocity u_s, following the gas dynamics considerations for in-plane interaction in [26]:

$$u_\phi = \left(1 + \frac{u_s}{u_1}\right)\left[C_1 r + \frac{C_2}{r}\right] \tag{15}$$

where the tangential slip speed u_s is assumed to be proportional to $u_1 = \Omega_1 r_1$.

Fig. 2 shows the NSE cylindrical solution with the introduced modification. The cylindrical solution is slightly nonlinear, and it is compliant with the solution proposed in [30]. From [26], the tangential slip speed u_s is expressed as a function of the mean particle path λ:

$$u_s = \lambda r \frac{\partial\left(u_\phi / r\right)}{\partial r}. \tag{16}$$

Therefore, by combining the shear definition [30] with Eqs. (15) and (16), it yields

$$|\tau| = 2\mu \frac{C_2}{r_1^2}\left(1 + 2\lambda \frac{C_2}{r_1^2 u_1}\right)^{-1}. \tag{17}$$

Finally, substituting Eq. (12) in Eq. (17), it holds:

$$|\tau| = \rho \sqrt{\frac{2\bar{R}T}{\pi}} \Omega_1 r_1 \left(\frac{2\mathrm{Kn} C_0}{1 + 2\mathrm{Kn} C_0}\right). \tag{18}$$

If $\mathrm{Kn} \to 0$, Eq. (18) is consistent also in amplitude with Eq. (14). The calculation of the case with rotating external cylindrical surface i.e., $\Omega_1 = 0$ and $\Omega_2 \neq 0$, is left to the reader.

3.2. Annular laminar flow

As in Section 3.1, the NSE solution is discussed. Under continuum flow hypothesis, the radial wall shear stress at radius r is expressed by combining Eqs. (9) and (10):

$$\tau = \mu \frac{\Omega r}{d}. \tag{19}$$

The solution is compared with the in-plane NSE solution for non-null slip velocity [26]:

$$\tau = \mu \frac{\Omega r}{d}\left(1 + 2\frac{\lambda}{d}\right)^{-1}. \tag{20}$$

Eqs. (19) and (20) are compatible for continuum flow hypothesis, i.e., when $\mathrm{Kn} \to 0$. The drag torque T_1 is computed for a generic annular section of the wet surface bounded in r_1, r_2 with $r_2 > r_1$:

$$T_1 = \frac{1}{2}\rho \sqrt{2\pi \bar{R}T}\, \Omega \left(r_2^4 - r_1^4\right)\left(\frac{2\mathrm{Kn}}{1 + 2\mathrm{Kn}}\right). \tag{21}$$

3.3. Transient characterisation of windage power loss

Typically, power characterisation requires the experimental measurements of torque and speed in steady-state conditions. In FESS applications, steady-state conditions are not achievable since the input power is not controlled after the charging phase, resulting in self-discharge.

The FESS self-discharge is a transient behaviour in which the flywheel kinetic energy reduces due to friction, viscous interaction, aerodynamic effects, Eddy current, and contact losses. The self-discharge time of a FESS can be extended by reducing friction losses. For example, rolling bearings can be replaced with low-friction or magnetic interaction bearings.

In this section, a strategy to characterise windage power losses of FESS in self-discharge phase is proposed. By considering the FESS rotor operating in self-centring regime [47], the losses caused by the contact with backup bearings and the magnetic interaction are neglected. Therefore, the rotor power equilibrium is

$$I_p \dot{\Omega} \Omega = -\sum_j c_{w,j}\left(p, T\right) \Omega^{k_j + 1} \tag{22}$$

in which I_p is the rotor polar moment of inertia and $c_{w,j}\left(p, T\right)$ is the jth aerodynamic coefficient related to the drag torque contributions of a subset of rotor surfaces described by analytical and/or semi-empirical models.

A detailed list of angular speed exponents k_j is presented in Appendix.

An example calculation of the aerodynamic coefficient $c_{w,j}$ and corresponding k_j for an in-housing convex rotor is presented here. The rotor wet surface is modelled as cylindrical surface A and two identical circular surfaces B. Therefore, the total windage torque T_w can be expressed as a function of the moment coefficient C_M:

$$T_w = \rho \Omega_1^2 r_1^4 \left[\frac{1}{2}\pi C_{M_A} h + C_{M_B} r_1\right]. \tag{23}$$

Table 1
Case study characteristics.

Group	Property	Case study		
		1	2	3
Rotor test-rig geometry	r_1, rotor outer radius [m]	0.2120		1.075
	r_2, stator cavity radius [m]	0.2156		1.145
	h, rotor height [m]	0.121		1.0
	d_C, radial airgap [mm]	3.6	70	–
	d_D, axial airgap [mm]	12.3	180	–
Operating conditions	T_0, initial airgap temperature [° C]		25	
	Min. angular speed [rad/s]	1571		10.47
	Max. angular speed [rad/s]	4189		83.78
	Min. vacuum pressure [Pa]	$1.\bar{3}\times10^{1}$	10^{3}	–
	Max. vacuum pressure [Pa]	$1.\bar{3}\times10^{3}$		101325

The moment coefficients C_{M_A} and C_{M_B} are replaced with the models in Appendix, $\mathrm{Re}_{\phi m}$ and Re_{ϕ} from Eqs. (6) and (8). It yields:

$$T_w = \pi\mu r_1^3 \left[4\frac{h}{d}\frac{(1+G)^2}{(2+G)} + \frac{1}{G}\right]\Omega_1 = c_{w,j}\Omega_1^{k_j}. \tag{24}$$

The power loss characterisation can be performed in self-discharge phase by measuring Ω and $\dot{\Omega}$. Moreover, only the time histories of Ω and $\dot{\Omega}$ during which the self-centring regime occurs must be considered to avoid additional power loss contributions. The dependency of $c_{w,j}$ in Eq. (22) on operational conditions requires conducting the experimental tests at constant temperature and vacuum pressure to ensure accurate characterisation.

The aerodynamic coefficients c_w, j vary with flow regime and the corresponding moment coefficients C_M of each rotor wet surface. The aerodynamic coefficient variability must be evaluated for every rotor system. In this paper, the aerodynamic coefficients $c_{w,j}$ are assumed to be constant within the operational speed range and are determined using a weighted average of numerical windage power loss percentage. The effectiveness of this approach is discussed in Section 5.

4. Windage loss model validation

In this section, the proposed harmonised windage loss model is validated using several case studies from the literature.

Table 1 lists the main rotor characteristics and operative conditions of the proposed case studies [31,41]. The selected case studies encompassing various applications and boundary conditions, are used to validate the model prediction capability across a wide range of conditions. This is crucial because the flow regime for each rotor surface under different operative conditions is not known a priori. Moreover, the three case studies represent viable design solutions for FESS applications and operational conditions. Case study 1 [31] is a realistic mid-vacuum in-housing FESS application . Case studies 2 and 3 are low speed rotor applications in which turbulent regime is predominant [41]. Case study 3 represents the theoretical limit for the external cylindrical surface interaction in the absence of an airgap.

Fig. 3 shows the validation of the windage loss model using the case studies. The grey round markers are the experimental windage power losses from the literature, the black dots or markers are the predictions, while blue circles and red markers are the proposed predictions using the harmonised windage loss model.

In the first case study, a high speed composite rotor with mid-vacuum level housing is studied [31]. Liu et al. noticed variations of radial airgap and a relevant rise in the rotor wet surface temperature ΔT due to aerodynamic heating. The Liu et al. prediction assumes that the flow is laminar and the temperature reaches a stationary condition on all the rotor wet surfaces.

Fig. 3(a) shows the comparison with [31]. The harmonised windage loss model allows to distinguish the predictions for the flow regime of the surfaces. The flow regime distinction is consistent with the increase in vacuum pressure, and the corresponding increase in Re_{ϕ} and $\mathrm{Re}_{\phi m}$. This result is not compatible with the Liu et al. assumption.

The laminar flow is only guaranteed at $1.\bar{3}\times10^{1}$ Pa. The proposed prediction is conservative and more precise than [31]: the reference prediction maximum experimental relative error is 13%, while the proposed prediction is 6.1%. Similarly, the $1.\bar{3}\times10^{2}$ Pa tests at low speed are well predicted: the reference prediction maximum experimental relative error is 18%, while the harmonised model prediction is 9.2%. In tests 6 and 8 at 4189 rad/s the prediction is not conservative.

The second case study is based on low-speed gyroscope energy harvester results [41].

The flow is turbulent in the tested conditions for the majority of the interacting surfaces, due to the rotor outer radius and the large airgaps (see Table 1).

Fig. 3(b) shows the performed comparison for both the datasets.

The model underestimates the experimental evidence, and it is more consistent at high speeds: the experimental relative error is 14% at 10.47 rad/s, −2% at 52.36 rad/s, while the reference prediction experimental relative error is 9%. Also, the harmonised windage loss model generally overestimates the reference prediction: the reference prediction relative error is high at low speeds (42% at 20.94 rad/s), while is more consistent at high speeds (8.3% at 83.78 rad/s).

The consistency of the proposed model is optimal. In FESS application, the high relative errors at low speeds are less important, while the strong correlation at low vacuum pressure and high speeds can be considered more significant.

In the third case study, the previous rotor is studied in free environment and atmospheric pressure. Fig. 3(c) shows the comparison of the proposed prediction with the experimental data and predictions of [41].

Again, the consistency of the proposed methodology is validated at high speeds. The predictions slightly underestimate the experimental data.

5. Flywheel energy storage system case study

An experimental validation activity is performed on the vertical rotor test-rig shown in Fig. 4. The aim of the test-rig is to investigate typical features of FESS, as shown in Fig. 4(a):

- parametric Passive Magnetic Bearings (PMB) interaction: the radial forces are supplied by the interaction of annular NdFeB magnets [48] with axial magnetisation. The proposed stator–rotor magnet configuration allows to generate a vertical compensation force. The radial and vertical bearing characteristics are tuned by changing the vertical position of stator magnets by acting on two upper and lower knobs;

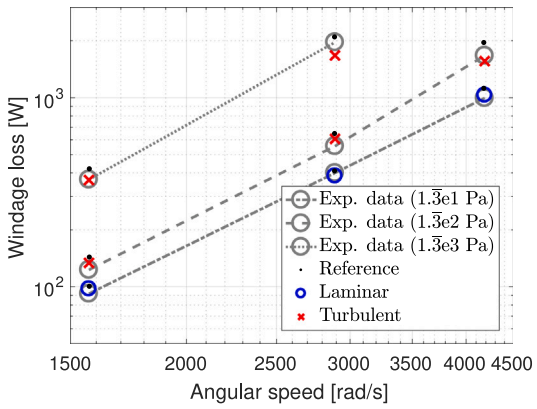

(a) Case study 1.

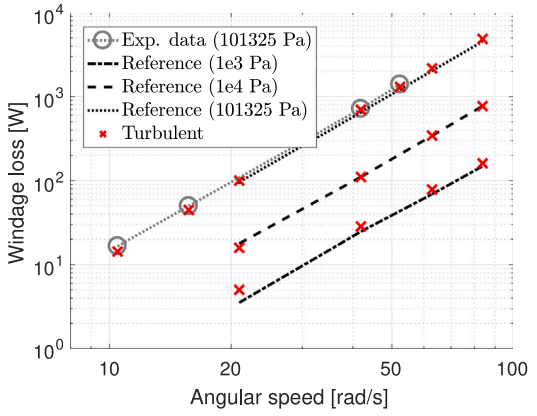

(b) Case study 2.

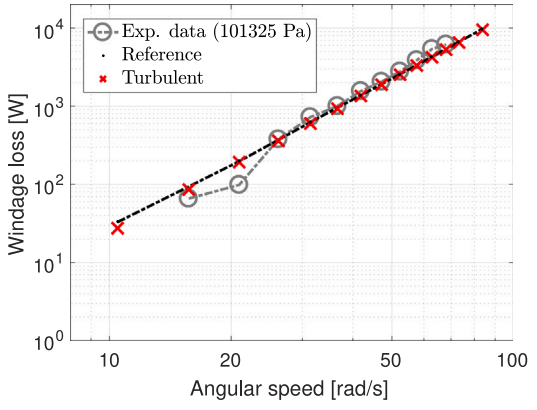

(c) Case study 3.

Fig. 3. Validation of the steady-state windage loss prediction.

- backup bearings: the radial rotor displacement is limited by Delrin bushings at upper and lower rotor sections;
- thrust low-friction contact bearing: the stability at null speed is guaranteed by a sphere-to-plane bearing. The reduced contact region allows to minimise the friction loss, making it a low-cost solution for FESS applications. The solution is inspired by Siebert et al. [49] i.e., a PMB horizontal flywheel demonstrator which overcomes the Earnshaw's theorem [50] limitations with an extra constraint supplied by a thrust jewel bearing. The concept is also present in the floating pen demonstrator, analysed in [51];
- electro-mechanical coupling: the kinetic energy is supplied by coupling the rotor to an external DC motor through an Electro-Magnetic (EM) clutch (see Fig. 4(a)). The clutch is connected during the charging phase and disconnected in the self-discharge phase.

Fig. 4(b) shows the vertical rotor test-rig architecture and the distribution of airgaps and Fig. 5 shows details about the low pressure experimental setup. The test-rig is placed inside a vacuum chamber. The power supply, acquisition and control connection are obtained by an electrical feedthrough on the chamber cover. The only acquired quantity is the radial displacement in correspondence of the upper rotor section, measured by a point-wise laser at high-frequency. The measurement is non-invasive and is used to evaluate the rotor contact with backup bearings, and also to estimate the rotor speed [52]. The acquisition is performed by LMS SCADAS Mobile together with Keyence LK-H152 i.e. displacement sensor using LMS Test.Lab at 4096 Hz.

From an aerodynamic point of view, the test-rig presents characteristics of both cylinder and annular configurations. Fig. 4(b) shows the typical distribution of airgap in operational conditions (light grey regions): the airgap aspect ratio G range is $0.085 \div 0.85$. The rotor presents multiple wet surfaces, assumed without housing, due to their very large airgaps. During operation, the EM clutch is disconnected and an airgap between the clutch plate and the rotor counterpart is generated. Moreover, the tuning of vertical and horizontal bearing characteristics by stator knobs implies a small variation of rotor annular surface airgaps. With the proposed configuration, all the harmonised windage loss models are implemented concurrently. The chamber temperature is supposed constant during the experimental activity at 22 °C. Measurements at the end of each test do not show significant variations. The pressure is experimentally kept constant by controlling the vacuum pump at several vacuum pressure levels. The possibility to control the vacuum pressure allows to validate the windage loss models at different regimes.

5.1. Numerical modelling

The test-rig power model presented in Eq. (22) includes an additional contribution to account for the low–friction contact point in the power equilibrium, i.e.,:

$$I_p \dot{\Omega} \Omega = -\mathrm{sgn}\left(\Omega\right) \mu_{f,d} r_c \left(mg - F_z\right) \Omega - \sum_j c_{w,j} \Omega^{k_j+1} \tag{25}$$

where $\mu_{f,d}$ is the dynamic friction coefficient for point-wise steel-steel rotational contact, mg is the rotor weight force, F_z is the vertical bearing compensation force, and r_c is the effective Hertzian contact radius.

The test-rig characteristics are known: rotor mass is 4.943 kg and moment of inertia 6.52×10^{-3} kg m^2. The dynamic friction coefficient $\mu_{f,d}$ is 0.1 in this application.

A sensitivity analysis of the test-rig windage power loss is performed to discuss the aerodynamic coefficient c_w variability. Fig. 6 shows the model windage loss variation versus vacuum pressure and speed. Overall, the angular speed has a more significant effect at higher pressures, which is mitigated at lower pressures. The change in behaviour is gradual with a definite transition in the extended pressure range $5 \times \left(10^2 \div 10^3\right)$ Pa. The reason of the transition is the change of flow regime of several surfaces of the rotor. Therefore, it is possible to predict a significant change in flow regime of the whole rotor and to direct the rotor geometry design to a selected windage loss level.

The windage power loss distribution is investigated among the dashed green curves i.e., feasible self-discharge testing conditions at constant vacuum level. In self-discharge phase, the flow regime of each rotor wet surface is dependent on the rotor angular speed and vacuum pressure. The singular contributions of surfaces in different

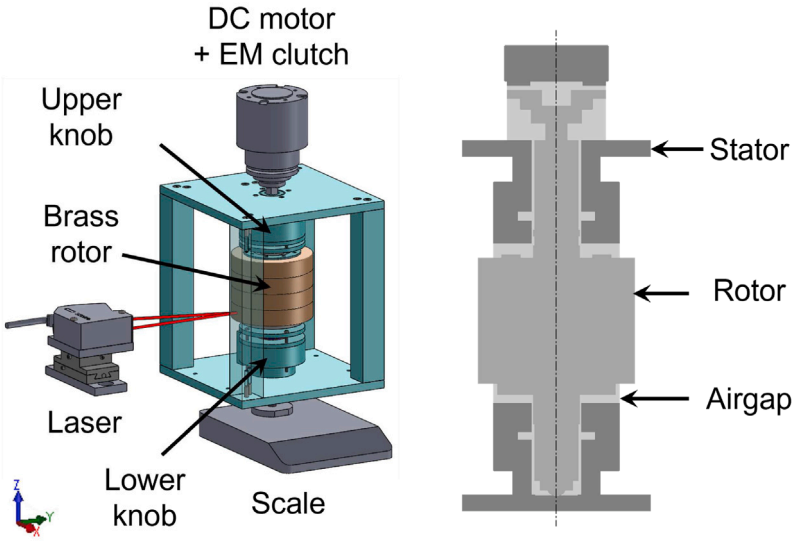

(a) Test-rig architecture. (b) Airgap distribution.

Fig. 4. Vertical rotor test-rig.

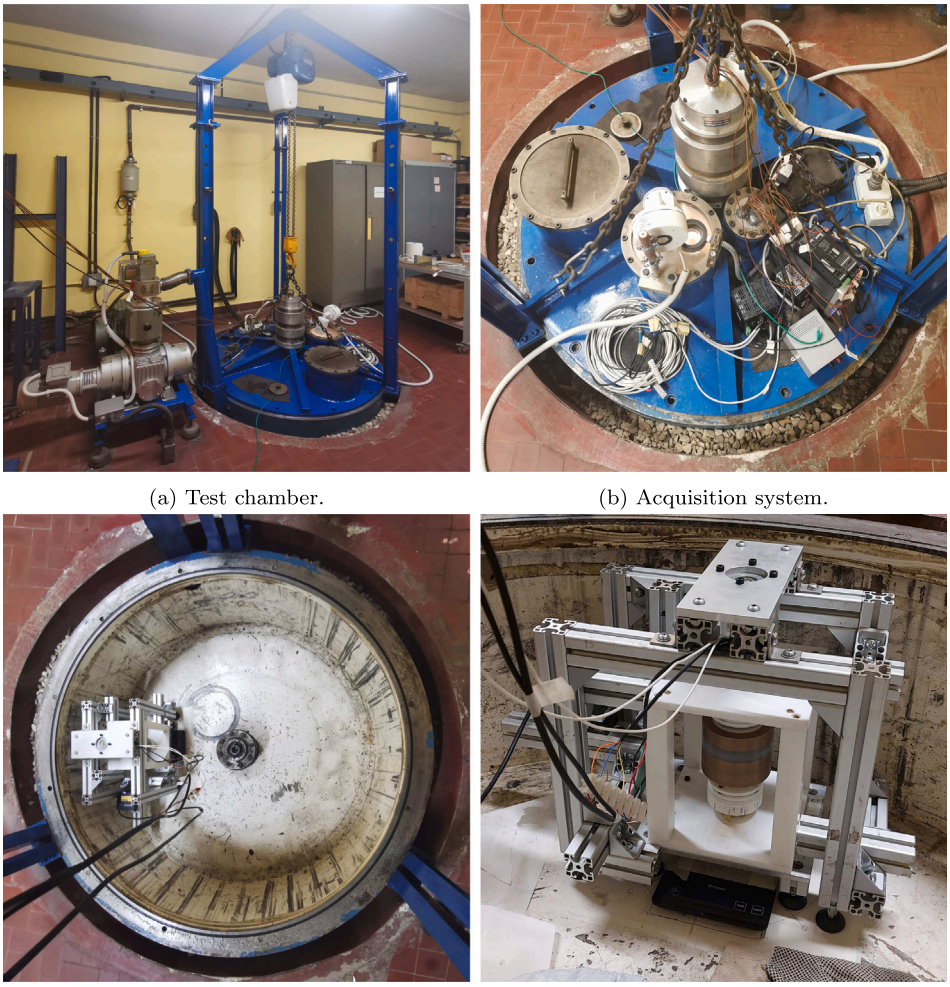

(a) Test chamber. (b) Acquisition system.

(c) Vacuum cavity test-rig arrangement. (d) Test-rig.

Fig. 5. Experimental setup for rotor windage loss evaluation at different vacuum pressure levels.

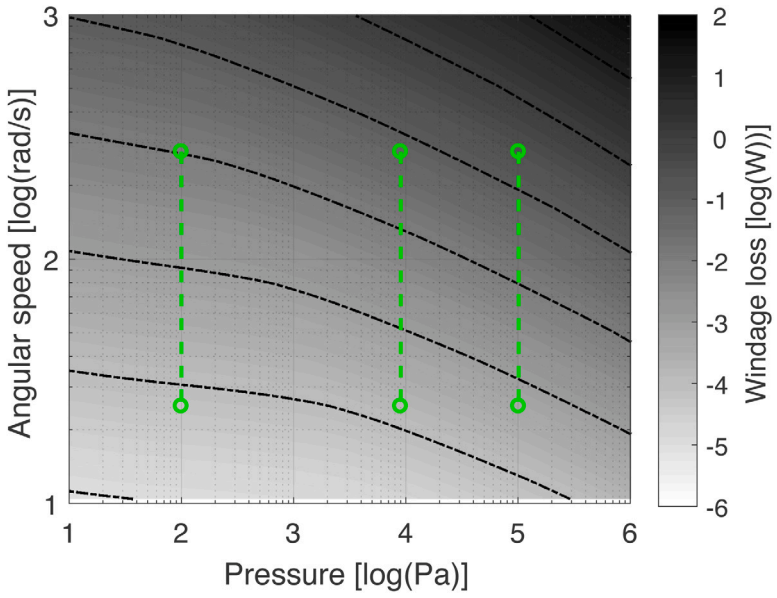

Fig. 6. Windage test comparison of results.

flow regimes are separated in order to distinguish their effects on the total windage losses. The separation of the contributions allows to identify critical surfaces generating higher windage losses.

Fig. 7 shows the coefficient c_w variations and the corresponding contributions on the overall windage power loss at the following vacuum levels: 101325 Pa at turbulent flow, 9×10^3 Pa, showing the transition to mixed flow, and 10^2 Pa mainly at laminar flow.

On the left side, the aerodynamic coefficients c_w are plotted versus speed, while the windage power loss weighted averaged c_w are plotted as black dash dot horizontal lines. On the right side, the windage loss contributions are plotted versus speed considering averaged c_w, the black dashed curve is the total averaged windage power loss $P_{w,mean}$ considering averaged c_w, while the black cross curve is the total windage power loss P_w considering variable c_w.

In Fig. 7(a), the aerodynamic coefficients have a large variability. The laminar flow aerodynamic coefficient $c_{w,0}$ is quite significant at low speeds, while completely negligible from about 80 rad/s. Also, the trend is monotonically decreasing: this phenomenon is physically explained as Reynolds number increases and gradually all the rotor wet surface flows pass from laminar to turbulent. The monotonic decrease in $c_{w,0}$ coincides with the increase in $c_{w,1}$ for cylindrical surfaces with small airgaps passing to transitional flow. Similarly, the monotonic decrease in $c_{w,3}$ mainly corresponds to cylindrical surfaces without airgaps passing to higher exponent semi-empirical turbulent flow models. The windage loss contributions show the significance of aerodynamic coefficients. At this pressure level, the flow regime is principally turbulent. The total windage loss is mainly due to cylinder surfaces in turbulent flow ($c_{w,2}$ and $c_{w,4}$), and marginally to cylinder surfaces in transitional flow ($c_{w,1}$).

In Fig. 7(b), the aerodynamic coefficient variability is smaller. The most significant aerodynamic coefficient variation occurs at $c_{w,1}$, $c_{w,3}$, and $c_{w,4}$ around 170 rad/s. The monotonic decrease in $c_{w,3}$ coincides with the abrupt increase in $c_{w,4}$ for cylindrical surfaces without airgaps passing to higher exponent semi-empirical turbulent flow models. At this pressure level, the flow regime is mainly low turbulent, while a significant portion of wet surfaces is in laminar flow. The total windage loss is mainly due to cylinder surfaces in low turbulent flow and disc surfaces in laminar flow ($c_{w,2}$ and $c_{w,3}$), while a more consistent portion of surfaces is in laminar flow ($c_{w,0}$). Additionally, cylinder surfaces without airgaps are still in turbulent flow and their contribution is more significant at high speeds ($c_{w,4}$).

In Fig. 7(c), the aerodynamic coefficients are constant. The laminar flow aerodynamic coefficients $c_{w,0}$ and $c_{w,2}$ are the only non-null coefficients describing flow regimes in the whole speed range. At this pressure level, the flow regime is completely laminar. The total windage loss is mainly due to cylinder and annular surfaces with airgaps in laminar flow ($c_{w,0}$), and secondly to annular surfaces without airgaps in laminar flow ($c_{w,2}$).

The power contributions lower than 1% are not reported.

The power loss contribution variation at vacuum levels is physically consistent: at atmospheric pressure, the turbulent flow is the most significant, while at lower pressures the turbulent flow contributions became marginal with respect to laminar one.

In conclusion, it is possible to describe the transient windage loss variation by considering constant aerodynamic coefficients. The possibility of adopting constant aerodynamic coefficients reduces the computational complexity of the prediction model and allows for effectively embedding aerodynamic losses in the design process. Also, for the proposed test-rig, the number of terms in the right hand side of Eq. (25) can be reduced to the most significant contributions listed in Table 2.

5.2. Experimental campaign

The experimental campaign is dedicated to characterise the test-rig windage losses at different vacuum pressure levels. The Design of Experiments (DoE) considers the rotor's vertical reaction to distinguish friction losses from the windage losses. The DoE parameters are:

- vacuum pressure: imposed by vacuum pump control at 101325 Pa, 9×10^3 Pa, and 10^2 Pa;
- thrust bearing compensation force: each configuration is imposed by acting together on upper and lower rotor knobs, and by measuring the vertical reaction force with a scale (see Fig. 4(a)). Three compensation levels are tested for different ranges of measured vertical reaction force: configuration A (minimum compensation) 45.1 ÷ 46.1 N, configuration B (intermediate compensation 24.5 ÷ 28.4 N, and configuration C (maximum compensation) 5.89 ÷ 10.1 N.

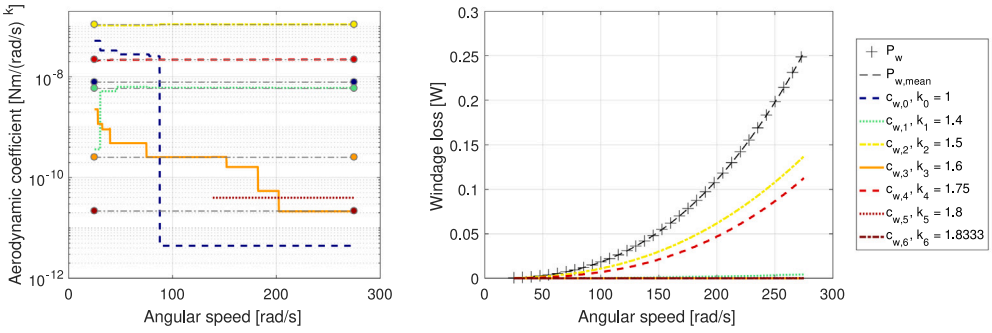

(a) Atmospheric pressure (101325 Pa).

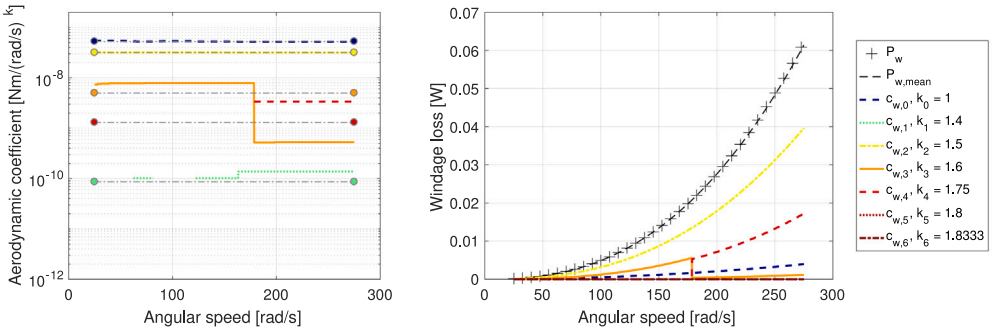

(b) Low-vacuum pressure (9×10^3 Pa).

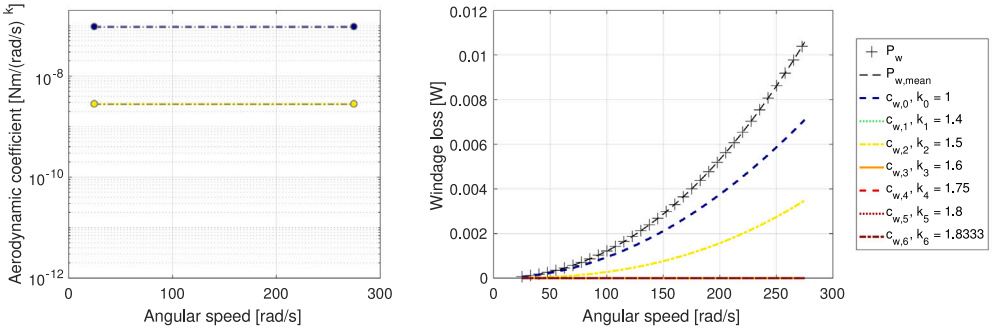

(c) Mid-vacuum pressure (1×10^2 Pa).

Fig. 7. Windage loss analysis: aerodynamic coefficient c_w trends (left) and windage power loss contributions (right).

Table 2
Averaged aerodynamic coefficients.

Vacuum pressure	Coefficients/Windage loss percentage					
	101325 Pa		9×10^3 Pa		10^2 Pa	
$c_{w,0}$	–	–	5.4×10^{-9}	8.28%	9.0×10^{-8}	66.8%
$c_{w,1}$	6.0×10^{-9}	1.31%	–	–	–	–
$c_{w,2}$	2.0×10^{-7}	71.2%	4.2×10^{-8}	70.2%	3.9×10^{-9}	33.2%
$c_{w,3}$	–	–	7.4×10^{-9}	13.0%	–	–
$c_{w,4}$	2.2×10^{-8}	26.9%	3.4×10^{-9}	8.46%	–	–

Table 3
Experimental campaign characteristics.

Group	Property	Configuration		
		A	B	C
Rotor test-rig geometry	r, max rotor outer radius [m]	0.05		
	h, rotor height [m]	0.255		
	d_C, min radial airgap [mm]	1		
	d_D, min axial airgap [mm]	1.25		
Operating conditions	T_0, airgap temperature [° C]	22		
	Min. angular speed [rad/s]	6		
	Max. angular speed [rad/s]	300		
	Vacuum pressure [Pa]	101325, 9×10^3, 10^2		
	F_z Vertical compensation force [N]	45.1 ÷ 46.1	24.5 ÷ 28.4	5.89 ÷ 10.1

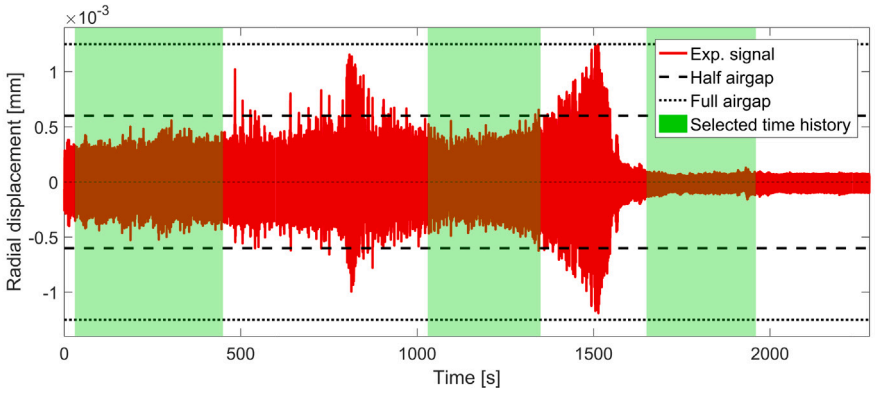

(a) Time signal segment selection.

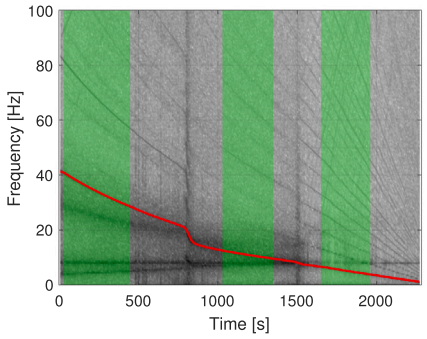

(b) Angular speed extrapolation from time–frequency analysis.

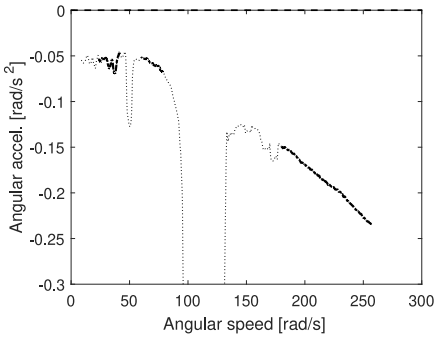

(c) Angular acceleration by numerical derivative.

Fig. 8. Rotor radial displacement post-processing procedure.

The boundary conditions and the initial conditions are listed in Table 3.

The experimental tests are performed accelerating the rotor up to 300 rad/s, then disengaging the EM clutch and letting the rotor to decelerate, while recording the laser radial displacements. The acquisitions are stopped when the rotor speed reaches 6 rad/s.

5.3. Numerical-experimental comparison

In this section, the harmonised windage loss model prediction is compared to the experimental results.

During the acquisition, the angular speed is monitored through the real-time Power Spectral Density (PSD) of the radial displacement with frequency resolution of 0.4 Hz. The lowest moving peak with larger amplitude corresponds to the rotor speed. The acquisitions are stopped when the PSD fundamental harmonic reaches 1 Hz.

After the experimental test, the radial displacement time history is post-processed to extrapolate the rotor speed and acceleration.

The rotor speed is computed by tracking the fundamental harmonic on the Fast Fourier Transform (FFT) spectrogram of the signal.

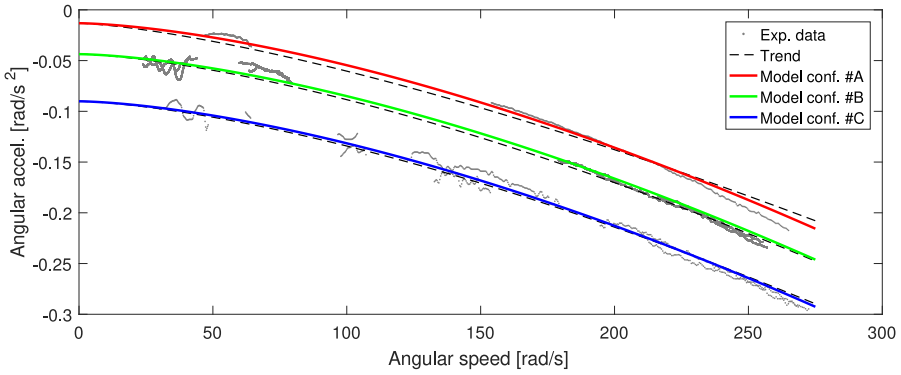

(a) Atmospheric pressure (101325 Pa).

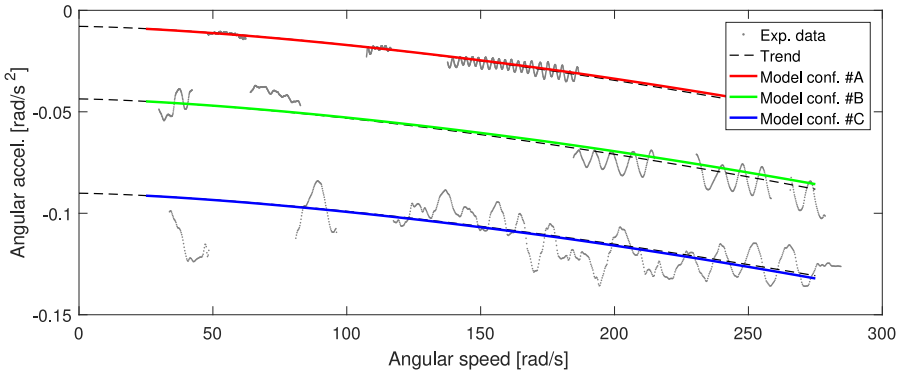

(b) Low-vacuum pressure (9×10^3 Pa).

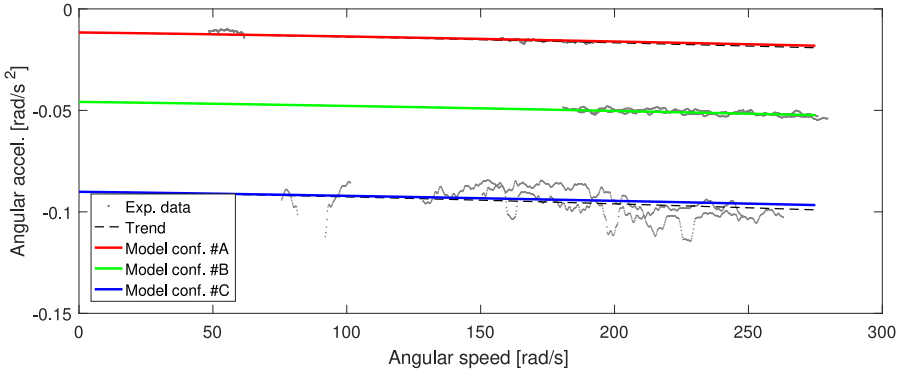

(c) Mid-vacuum pressure (10^2 Pa).

Fig. 9. Numerical-experimental comparison of rotor speed-acceleration relationship.

Fig. 8 summarises the post-processing procedure steps, based on consolidated signal processing techniques in time and frequency domains. The radial displacement signal is segmented and considered only when is limited to 0.6 mm i.e., half of the cylindrical minimum airgap. Fig. 8(a) shows different green regions of the considered signal time history segments. The red curve is the time-speed characteristics. Fig. 8(b) shows the FFT spectrogram of the whole radial displacement signal, where darker regions have high signal power density content. Finally, the angular acceleration is obtained by numerical differentiation of the angular speed. Fig. 8(c) shows the comparison between the whole speed–acceleration characteristics in black dot curve, and the selected segments in red colour.

The selected time segments share a common slope, unaffected by power loss mechanisms other than windage and friction. The contribution of friction losses depends on vertical compensation level and is observed in Fig. 8(c) as a non-null acceleration when the rotor speed is null.

In Fig. 9, the harmonised windage loss model is compared to the post-processed data. The grey markers represent the post-processed experimental data segments, the black dashed curves are the data trends obtained by fitting the speed polynomial law to the experimental data. Red, green, and blue solid curves are the predictions of the windage loss model.

Fig. 9(a) shows the validation at atmospheric pressure. The predicted behaviour at three levels of vertical compensation differs only

Table 4
Numerical-experimental comparison.

Configuration	Vacuum pressure [Pa]	RMSEP trend vs. Exp. data [%]	RMSEP model vs. trend [%]
A	101 325	5.3	2.6
	9×10^3	7.1	1.3
	1×10^2	3.1	3.2
B	101 325	1.7	2.0
	9×10^3	6.5	2.4
	1×10^2	1.8	0.1
C	101 325	4.9	1.3
	9×10^3	9.0	0.6
	1×10^2	6.3	1.5

in the acceleration offset. The model optimally predicts the windage loss behaviour at speeds far from critical speeds but underestimates at high speeds, as previously noticed in Section 4.

Fig. 9(b) shows the validation at 9×10^3 Pa. The prediction is correctly aligned to data trends. The prediction is almost horizontal, since the friction loss contribution is the most significant.

Fig. 9(c) shows the validation at 10^2 Pa. The prediction is almost linear, since the behaviour is mainly in laminar flow.

The performance of the developed prediction model are quantified by computing the Root Mean Square Error of Prediction (RMSEP) between the datasets with the following definition:

$$\mathrm{RMSEP} = \sqrt{\frac{\sum_{i=1}^{n} \left(\frac{x_{i,\mathrm{ref}} - x_i}{x_{i,\mathrm{ref}}} \right)^2}{n}} \tag{26}$$

where n is the number of samples per configuration and prescribed vacuum pressure, x_i and $x_{i,\mathrm{ref}}$ are the ith samples of the studied and reference datasets, respectively. Table 4 lists the computed RMSEP for all the configurations studied in the DoE. The scattering in experimental data affects the RMSEP between trend curves and experimental data. Instead, the trend represents the fitted solution by optimising the $c_{w,j}$ coefficients. The RMSEP between trend curves and experimental data is globally lower than 10%. Also, the highest RMSEP between the model results and the trend curves is 3.2%.

6. Conclusions

In this paper, a procedure for FESS windage loss characterisation is proposed. The characterisation procedure relies on describing windage loss contributions from fluid interactions with cylindrical and annular surfaces, considering different airgaps, operational conditions and flow regimes. This is achieved through indirect measurements of angular speed during self-discharge transient conditions.

The windage losses are deeply investigated, by the analytical and semi-empirical models in case of temperature, pressure, airgap, and speed variability. The windage loss model is obtained by collecting analytical and semi-empirical formulations in the literature and by introducing corrections for free molecule flow, typical of high vacuum levels.

The loss model is validated in steady–state conditions using case studies from the literature. It is shown that the developed windage loss model is in agreement with experimental case studies at high speeds and low pressure levels.

An experimental test-rig is developed to validate the windage loss model and the characterisation procedure. The test-rig exploits laser radial measurements to obtain non-invasive angular speed and acceleration estimations. The numerical–experimental validation is performed at different vacuum levels, showing optimal correlation up to 270 rad/s and 10^2 Pa. The proposed methodology presents limitations: the model can be only used for almost stationary behaviour since the temperature of the system is considered constant in time. Also, the whole geometry is assumed axisymmetric and only representable by cylinders and discs. The limitations are compatible with FESS application, since temperature rising is mainly caused by aerodynamic heating, which is marginal in high vacuum. The developed model will be used in rotor design frameworks to optimise rotor topology, aiming at reducing windage losses and vacuum requirements.

CRediT authorship contribution statement

Simone Venturini: Writing – original draft, Validation, Methodology, Investigation, Formal analysis, Data curation, Conceptualization. **Salvatore Paolo Cavallaro:** Visualization, Software, Data curation, Conceptualization. **Alessandro Vigliani:** Writing – review & editing, Supervision, Resources, Project administration, Methodology, Funding acquisition, Conceptualization.

Declaration of competing interest

The authors declare that they have no known competing financial interests or personal relationships that could have appeared to influence the work reported in this paper.

Data availability

Data will be made available on request.

Acknowledgements

This research was developed within the “Network 4 Energy Sustainable Transition – NEST” project. The “NEST” project is funded under the Italian National Recovery and Resilience Plan (NRRP), Mission 4 Component 2 Investment 1.3 - Call for tender No. 1561 of 11.10.2022 of Ministero dell’Università e della Ricerca (MUR) and the European Union – NextGenerationEU consortium.

The authors express their gratitude to Prof. Nicola Amati for the opportunity of conducting the experimental campaign at the Flywheel Test Facility at the Department of Mechanical and Aerospace Engineering (DIMEAS) of the Politecnico di Torino.

Appendix. Analytical and semi-empirical models

The models for cylinder and disc surfaces interactions are listed in Tables A.5 and A.6. The moment coefficients C_M, the type of models, and the angular speed exponent k for windage torque contributions are listed.

The models marked by “*” in Table A.5 have been developed by fitting polynomial laws to Theodorsen and Regier’s closed-form model [44] of turbulent flow around a cylinder with housing. The proposed models produce moments coefficients C_M with a maximum relative error of 5% compared to the Theodorsen and Regier model. Their usage is necessary to maintain the whole windage power loss model in polynomial form.

Unlike in the literature, the range of Reynolds and Taylor numbers for the applications is not reported. The effective flow regime is the largest C_M for prescribed aspect ratio G and Re_ϕ or $\mathrm{Re}_{\phi m}$. The calculation procedure is graphically represented in Figs. A.10 and A.11.

The regions of applicability of each model listed in Table A.5 and A.6 are shown. In case of surface interaction with housing, the aspect ratio G is also considered; instead, free environment surface interactions depend only on Reynolds numbers.

Table A.5
Moment coefficients for cylinder surface interactions: Taylor and Reynolds classifications.

Interaction	Flow regime	Moment coefficient C_M	Model	Torque
Cylinder with housing	Laminar (Linear) [30,42]	$8\frac{(1+G)^2}{(2+G)}\mathrm{Re}_{\phi m}^{-1}$	NSE	$T \propto \Omega^1$
	Laminar [25,30,42,43]	$10\ G^{0.3}\mathrm{Re}_{\phi m}^{-1}$	Empirical	
	Laminar with vortexes [25,42,43]	$2\ (2+G)\left[1+1.4472\left(1-\frac{41.3^2}{G\mathrm{Re}_{\phi m}^2}\right)\right]\mathrm{Re}_{\phi m}^{-1}$		
	Transitional [30,42]	$2\ G^{0.3}\mathrm{Re}_{\phi m}^{-0.6}$		$T \propto \Omega^{1.4}$
	Turbulent (low) [30,42]	$1.03\ G^{0.3}\mathrm{Re}_{\phi m}^{-0.5}$		$T \propto \Omega^{1.5}$
	Turbulent [30,42]	$0.065\ G^{0.3}\mathrm{Re}_{\phi m}^{-0.2}$		$T \propto \Omega^{1.8}$
	Turbulent (high) [25]	$0.12\ G^{0.4}\mathrm{Re}_{\phi m}^{-0.2}$		
Cylinder without housing	Laminar [44]	$4\ \mathrm{Re}_{\phi}^{-1}$	NSE	$T \propto \Omega^1$
	Turbulent [44]	$C_M^{-0.5} = -0.6 + 4.07\log(\mathrm{Re}_{\phi}C_M^{0.5})$	Empirical	–
	Turbulent I*	$0.442\ \mathrm{Re}_{\phi}^{-0.5}$		$T \propto \Omega^{1.5}$
	Turbulent II*	$0.257\ \mathrm{Re}_{\phi}^{-0.4}$		$T \propto \Omega^{1.6}$
	Turbulent III*	$0.079\ \mathrm{Re}_{\phi}^{-0.25}$		$T \propto \Omega^{1.75}$
	Turbulent IV*	$0.029\ \mathrm{Re}_{\phi}^{-0.1\bar{6}}$		$T \propto \Omega^{1.8\bar{3}}$

Table A.6
Moment coefficients for disc surface interactions: Reynolds classification.

Interaction	Flow regime	Moment coefficient C_M	Model	Torque
Disc with housing	Laminar I [45]	$\pi\ G^{-1}\mathrm{Re}_{\phi}^{-1}$	NSE	$T \propto \Omega^1$
	Laminar II [45]	$1.85\ G^{0.1}\mathrm{Re}_{\phi}^{-0.5}$	Empirical	$T \propto \Omega^{1.5}$
	Turbulent III [45]	$0.04\ G^{-0.1\bar{6}}\mathrm{Re}_{\phi}^{-0.25}$		$T \propto \Omega^{1.75}$
	Turbulent IV [45]	$0.051\ G^{0.1}\mathrm{Re}_{\phi}^{-0.2}$		$T \propto \Omega^{1.8}$
Disc without housing	Laminar [27,29]	$3.87\ \mathrm{Re}_{\phi}^{-0.5}$	Empirical	$T \propto \Omega^{1.5}$
	Turbulent [27,29]	$0.146\ \mathrm{Re}_{\phi}^{-0.2}$		$T \propto \Omega^{1.8}$

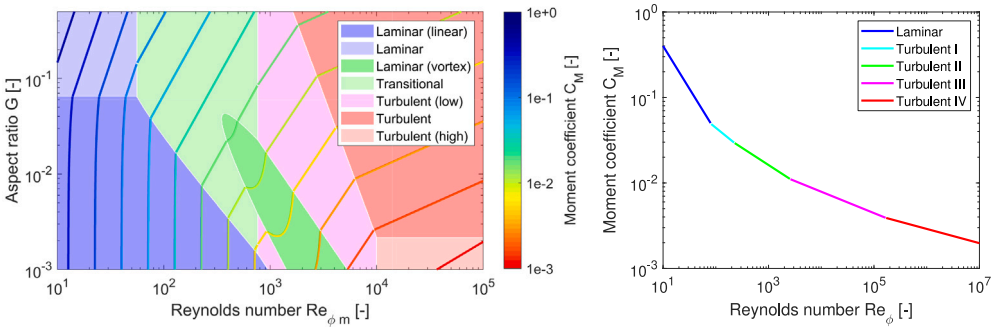

Fig. A.10. Flow regimes of cylindrical surface: cylinder with housing (left) and without housing (right).

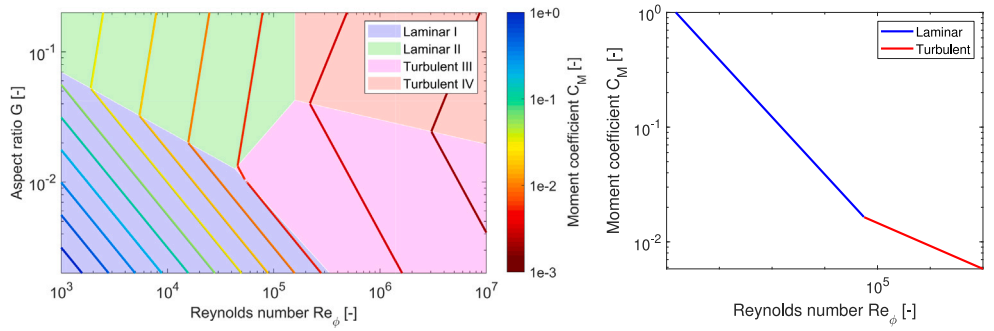

Fig. A.11. Flow regimes of circular surface: disc with housing (left) and without housing (right).

References

[1] Li X, Palazzolo A. A review of flywheel energy storage systems: state of the art and opportunities. J Energy Storage 2022;46:103576. http://dx.doi.org/10.1016/j.est.2021.103576.

[2] Arseneaux J. 20 MW flywheel frequency regulation plant. Tech. rep, USDOE Office of Energy Efficiency and Renewable Energy (EERE); 2015, http://dx.doi.org/10.2172/1351296.

[3] Lei M, Meng K, Feng H, Bai J, Jiang H, Zhang Z. Flywheel energy storage controlled by model predictive control to achieve smooth short-term high-frequency wind power. J Energy Storage 2023;63:106949. http://dx.doi.org/10.1016/j.est.2023.106949.

[4] Hamsic N, Schmelter A, Mohd A, Ortjohann E, Schultze E, Tuckey A, et al. Increasing renewable energy penetration in isolated grids using a flywheel energy storage system. In: 2007 International conference on power engineering, energy and electrical drives. 2007, p. 195–200. http://dx.doi.org/10.1109/POWERENG.2007.4380112.

[5] Boukettaya G, Krichen L, Ouali A. A comparative study of three different sensorless vector control strategies for a flywheel energy storage system. Energy 2010;35(1):132–9. http://dx.doi.org/10.1016/j.energy.2009.09.003.

[6] Miyazaki Y, Mizuno K, Yamashita T, Ogata M, Hasegawa H, Nagashima K, et al. Development of superconducting magnetic bearing for flywheel energy storage system. Cryogenics 2016;80:234–7. http://dx.doi.org/10.1016/j.cryogenics.2016.05.011, Special Issue on HTS Cooling 2015.

[7] Suzuki Y, Koyanagi A, Kobayashi M, Shimada R. Novel applications of the flywheel energy storage system. Energy 2005;30(11):2128–43. http://dx.doi.org/10.1016/j.energy.2004.08.018.

[8] Hearn C, Flynn M, Lewis M, Thompson R, Murphy B, Longoria RG. Low cost flywheel energy storage for a fuel cell powered transit bus. In: 2007 IEEE vehicle power and propulsion conference. 2007, p. 829–36. http://dx.doi.org/10.1109/VPPC.2007.4544239.

[9] Wagner R, Jansen R. Flywheel technology development at the NASA Glenn research center. In: Electrical energy storage systems applications and technologies (EESAT) conference proceedings. 2002, p. 6.

[10] Abdi B, Alimardani A, Ghasemi R, Mirtalaei SMM. Energy storage selection for LEO satellites. Int J Mach Learn Comput 2013;3:287–90. http://dx.doi.org/10.7763/IJMLC.2013.V3.322.

[11] Zajac J, Zacek F, Lejsek V, Brettschneider Z. Short-term power sources for tokamaks and other physical experiments. Fusion Eng Des 2007;82(4):369–79. http://dx.doi.org/10.1016/j.fusengdes.2007.03.005.

[12] Rendell D, Shaw SR, Pool PJ, Oberlin-Harris C. Thirty year operational experience of the JET flywheel generators. Fusion Eng Des 2015;98–99:1140–3. http://dx.doi.org/10.1016/j.fusengdes.2015.06.049, Proceedings of the 28th Symposium On Fusion Technology (SOFT-28).

[13] Mitali J, Dhinakaran S, Mohamad A. Energy storage systems: a review. Energy Storage Saving 2022;1(3):166–216. http://dx.doi.org/10.1016/j.enss.2022.07.002.

[14] Dever T. Development of a high specific energy flywheel module, and studies to quantify its mission applications and benefits. In: Annual IEEE energyTech conference. (E-664039):2013, p. 19.

[15] Toh C-S, Chen S-L. Design, modeling and control of magnetic bearings for a ring-type flywheel energy storage system. Energies 2016;9(12):1051. http://dx.doi.org/10.3390/en9121051.

[16] Rastegarzadeh S, Mahzoon M, Mohammadi H. A novel modular designing for multi-ring flywheel rotor to optimize energy consumption in light metro trains. Energy 2020;206:118092. http://dx.doi.org/10.1016/j.energy.2020.118092.

[17] BeaconPower BP400 datasheet. 2014, URL https://beaconpower.com, BeaconPower BP400 datasheet, available in 2024-02-29.

[18] PowerThru UPS technical paper. 2016, URL http://power-thru.com, PowerThru UPS technical paper, available in 2024-02-29.

[19] GKN gyrodrive Mk4 datasheet. 2013, URL https://www.apcuk.co.uk/impact/case-studies/gkn-gyrodrive/, GKN Gyrodrive Mk4 datasheet, available in 2024-02-29.

[20] Quurck L, Richter M, Schneider M, Franz D, Rinderknecht S. Design and practical realization of an innovative flywheel concept for industrial applications. Technische Mech-Eur J Eng Mech 2017;37(2–5):151–60. http://dx.doi.org/10.24352/UB.OVGU-2017-092.

[21] Li X, Anvari B, Palazzolo A, Wang Z, Toliyat H. A utility-scale flywheel energy storage system with a shaftless, hubless, high-strength steel rotor. IEEE Trans Ind Electron 2018;65(8):6667–75. http://dx.doi.org/10.1109/TIE.2017.2772205.

[22] Liu H-P, Werst M, Hahne J, Bogard D. Investigation of windage splits in an enclosed test fixture having a high speed composite rotor in low air pressure environments. In: 2004 12th Symposium on electromagnetic launch technology. 2004, p. 223–8. http://dx.doi.org/10.1109/ELT.2004.1398078.

[23] Kolk M. Ein schwungrad-energiespeicher mit permanentmagnetischer lagerung. In: Berichte des Forschungszentrums Jülich, vol. 3470, (no. Juel-3470):Jülich: Forschungszentrum Jülich GmbH Zentralbibliothek, Verlag; 1997, p. 139, URL https://juser.fz-juelich.de/record/863304.

[24] Baldissera P. Proposal of a coast–down model including speed-dependent coefficients for the retarding forces. Proc Inst Mech Eng Part P: J Sports Eng Technol 2017;231(2):154–63. http://dx.doi.org/10.1177/1754337116658587.

[25] Schlichting H. Boundary–layer theory. New York: MacGraw Hill; 1979.

[26] Vincenti WG, Kruger CH. Introduction to physical gas dynamics. New York: Wiley; 1965.

[27] Genta G. Kinetic energy storage. Butterworth-Heinemann; 1985.

[28] Gu A. On the viscous drag on a rotating disk. J Fluids Eng 1974;96(2):184–6. http://dx.doi.org/10.1115/1.3447127.

[29] Schlichting H, Gersten K. Boundary–layer theory. Berlin, Heidelberg: Springer; 2017, http://dx.doi.org/10.1007/978-3-662-52919-5.

[30] Childs PR. Rotating flow. Oxford: Butterworth-Heinemann; 2010, http://dx.doi.org/10.1016/C2009-0-30534-6.

[31] Liu H-P, Werst M, Hahne JJ, Bogard D. Prediction of windage losses of an enclosed high speed composite rotor in low air pressure environments. In: Proceedings of the ASME 2003 heat transfer summer conference. Heat transfer summer conference, vol. Heat Transfer: Volume 1, 2003, p. 15–23. http://dx.doi.org/10.1115/HT2003-47118.

[32] Hahne J, Werst M, Penney C, Liu H-P, O'Rarden J, Bogard D. Measurement of windage losses and temperature distribution for a high speed composite rotor in a stator assembly at low air pressures. In: Proceedings of the ASME 2003 heat transfer summer conference. Heat transfer summer conference, vol. Heat Transfer: Volume 1, 2003, p. 7–14. http://dx.doi.org/10.1115/HT2003-47117.

[33] Ertz G, Twiefel J, Krack M. Feasibility study for small scaling flywheel-energy-storage systems in energy harvesting systems. Energy Harvesting Syst 2014;1(3–4):233–41. http://dx.doi.org/10.1515/ehs-2013-0010.

[34] Barkova AA, Pugachuk AS. Application of computational gas dynamics methods for calculating losses during rotation of solids in low vacuum conditions. J Phys Conf Ser 2021;2057(1):012019. http://dx.doi.org/10.1088/1742-6596/2057/1/012019.

[35] Wei C, Xu Y, Zhang K, Lv C, Dong X, Zhang S, et al. Research on windage losses of smooth rotor supported by active magnetic bearings in a vacuum chamber. Vacuum 2019;159:76–81. http://dx.doi.org/10.1016/j.vacuum.2018.10.006.

[36] Amiryar ME, Pullen KR. Analysis of standby losses and charging cycles in flywheel energy storage systems. Energies 2020;13(17). http://dx.doi.org/10.3390/en13174441.

[37] Skinner M, Mertiny P. Experimental characterization of low-speed passive discharge losses of a flywheel energy storage system. Appl Mech 2021;2(1):1–15. http://dx.doi.org/10.3390/applmech2010001.

[38] Eltaweel M, Herfatmanesh MR. Analysis of standby power in an enclosed high-speed flywheel energy storage system using the CFD-ANOVA approach. In: 2023 JSAE/SAE powertrains, energy and lubricants international meeting. Society of Automotive Engineers of Japan; 2023, http://dx.doi.org/10.4271/2023-32-0069.

[39] Motaman S, Eltaweel M, Herfatmanesh MR, Knichel T, Deakin A. Numerical analysis of a flywheel energy storage system for low carbon powertrain applications. J Energy Storage 2023;61:106808. http://dx.doi.org/10.1016/j.est.2023.106808.

[40] Pozzi N, Bonfanti M, Mattiazzo G. Mathematical modeling and scaling of the friction losses of a mechanical gyroscope. Int J Appl Mech 2018;10(3). http://dx.doi.org/10.1142/S1758825118500242.

[41] Sirigu AS, Gallizio F, Giorgi G, Bonfanti M, Bracco G, Mattiazzo G. Numerical and experimental identification of the aerodynamic power losses of the ISWEC. J Marine Sci Eng 2020;8(1). http://dx.doi.org/10.3390/jmse8010049.

[42] Bilgen E, Boulos R. Functional dependence of torque coefficient of coaxial cylinders on gap width and Reynolds numbers. J Fluids Eng 1973;95(1):122–6. http://dx.doi.org/10.1115/1.3446944.

[43] Kaye J, Elgar EC. Modes of adiabatic and diabatic fluid flow in an annulus with an inner rotating cylinder. Trans Am Soc Mech Eng 1958;80(3):753–63. http://dx.doi.org/10.1115/1.4012502.

[44] Theodorsen T, Regier A. Experiments on drag of revolving disks, cylinders, and streamline rods at high speeds. Tech. rep, National Advisory Committee for Aeronautics (NACA); 1944.

[45] Daily JW, Nece RE. Chamber dimension effects on induced flow and frictional resistance of enclosed rotating disks. J Basic Eng 1960;82(1):217–30. http://dx.doi.org/10.1115/1.3662532.

[46] Iuso G, Virone G, Cafiero G, Bonisoli E, Lisitano D, Venturini S. Aeroelastic-structural coupling in antenna prototype for windy open-space. 8th International conference on computational methods for coupled problems in science and engineering, COUPLED PROBLEMS 2019 2021;481–92.

[47] Cavallaro SP, Vigliani A. Nonlinear dynamics of a vertical magnetic rotor. Tech. rep, 2024.

[48] Bonisoli E, Venturini S, Cavallaro SP. Nonlinear characterisation of a rotor on passive magnetic supports. Int J Mech Control 2022;23(1):121–8.

[49] Siebert M, Ebihara B, Jansen R, Fusaro RL, Morales W, Kascak A, et al. A passive magnetic bearing flywheel. In: 36th intersociety energy conversion engineering conference. NASA/TM-2002-211159, 2002, p. 1–10.

[50] Earnshaw S. On the nature of the molecular forces which regulate the constitution of the luminiferous ether. Trans Cambridge Philos Soc 1848;7:97.

[51] Cavallaro SP, Venturini S, Bonisoli E. Nonlinear dynamics of a horizontal rotor with asymmetric magnetic supports. Int J Non-Linear Mech 2024;104764. http://dx.doi.org/10.1016/j.ijnonlinmec.2024.104764.

[52] Bonisoli E, Dimauro L, Venturini S, Cavallaro SP. Experimental detection of nonlinear dynamics using a Laser profilometer. Appl Sci (Switzerland) 2023;13(5). http://dx.doi.org/10.3390/app13053295.